Spin Hall effect in two-dimensional InSe: Interplay between Rashba and Dresselhaus spin-orbit couplings

M. Umar Farooq [1], Lede Xian,[2] and Li Huang [1,*]

[1]*Department of Physics, Southern University of Science and Technology, Shenzhen, Guangdong 518055, China*

[2]*Songshan Lake Materials Laboratory, Dongguan, Guangdong 523808, China*

(Received 5 April 2022; revised 26 May 2022; accepted 2 June 2022; published 13 June 2022)

Materials with inversion asymmetries can exhibit strong spin Hall effect (SHE) in the presence of Dresselhaus and Rashba spin-orbit coupling (D/R SOC) interactions. Ideally, in a two-dimensional crystal, inversion asymmetry could be modulated by stacking order and external perturbations. Here, using first-principles calculations, we systematically investigate the interplay between DSOC and RSOC and their influences on SHE in mono- and bilayer InSe. We show that in the presence of DSOC, the introduction of Rashba interaction through gate voltages in monolayer InSe increases Zeeman-like spin splitting around the Brillouin-zone center and contributes to the enhancement of spin Hall conductivity (SHC), which reaches a saturation point due to the RSOC-enforced spiral-spin texture. The SHC in the unperturbed centrosymmetric *AB* stacked bilayer shows a peak associated with the Mexican-hat-like valence-band edge; however, in a wide energy range the SHC stays insignificant. In the AB' stacked bilayer with the intrinsic RSOC present, the value of SHC can be comparable to that of *AB* stacked bilayer with an external electric field. Moreover, we show that the spin-momentum locking in the AB' stacked bilayer is switchable by a gate voltage. These findings provide a promising route for spintronic and magneto-optical applications by exploiting the rich physics of spin-orbit effects.

DOI: 10.1103/PhysRevB.105.245405

I. INTRODUCTION

A wide variety of nontrivial physical phenomena are triggered by relativistic spin-orbit coupling (SOC) in conjunction with crystal symmetries [1–4]. The most prominent examples are the anomalous Hall effect in crystals with broken time-reversal symmetry and its analogous spin Hall effect (SHE) in nonmagnetic materials [5,6], where an electric field induces a transverse spin current. It therefore paves an attractive way for fast and low-power switching of magnetization in spintronic devices, such as magnetic tunnel junctions [7]. Moreover, in the presence of a magnetic field, the interplay of Zeeman coupling and the spin-orbit interactions can give rise to resonance spin Hall conductance [8,9].

In crystalline solids, the SOC can be viewed as symmetry-allowed couplings between the spin orientations and the crystal momentum of the electron. There are essentially two types of SOC, namely, the Rashba term induced by structural inversion asymmetry and the Dresselhaus term arising from crystal inversion asymmetry. Previous efforts have mainly been devoted to the SHE in the noncentrosymmetric systems with Rashba SOC (RSOC) [10,11]. It has been recognized that Rashba and Dresselhaus SOC (DSOC) coexisting in a material can interfere with each other. However, existing theoretical calculations suffer from limitations. Although analytical modeling offers insights into the relationship between symmetry and SOC interactions, they are quite apart from the real physical system. On the other hand, most first-principles studies only focus on the role of a single type of SOC interactions, and the interplay between different types of SOC is rarely discussed [12–16].

Experimentally, it is difficult to tune the SOC interactions through reversible external perturbations in three-dimensional crystals. In this regard, layered van der Waals materials offer a perfect basis for engineering SOC via stacking order and gate voltages. Therefore, such layered materials can be promising platforms to explore the underlying physics of symmetry-allowed SOC interactions [17,18]. Here, we focus on the layered InSe systems due to their strong SOC and other unusual properties, such as a topmost valence band with a nonparabolic Mexican-hat shape, van Hove singularity, and exciting nonlinear optical properties [19–21].

The InSe monolayer is a noncentrosymmetric system, which can be transformed into an inversion-symmetric or asymmetric bilayer with different stacking orders [17,22]. Moreover, the structural asymmetry can also be tuned by employing gate voltages. Thus, InSe can be a good system for studying SHE in conjunction with R/DSOC interactions and symmetry. Using *ab initio* and maximally localized Wannier function (MLWF) calculations, we have studied the interplay of DSOC and RSOC interactions and their influence on SHE. We find that the pure DSOC interaction gives rise to a persistent out-of-plane spin texture. The spin Hall conductivity (SHC) can be enhanced by introducing RSOC. It is also shown that in the presence of DSOC, the introduction of RSOC contributes to SHC by shifting the splitting from the corners to the center of the Brillouin zone (BZ), but it does not induce additional momentum-dependent Zeeman-like spin splitting. The manipulation of spin texture in 2D materials provides a

*huangl@sustech.edu.cn

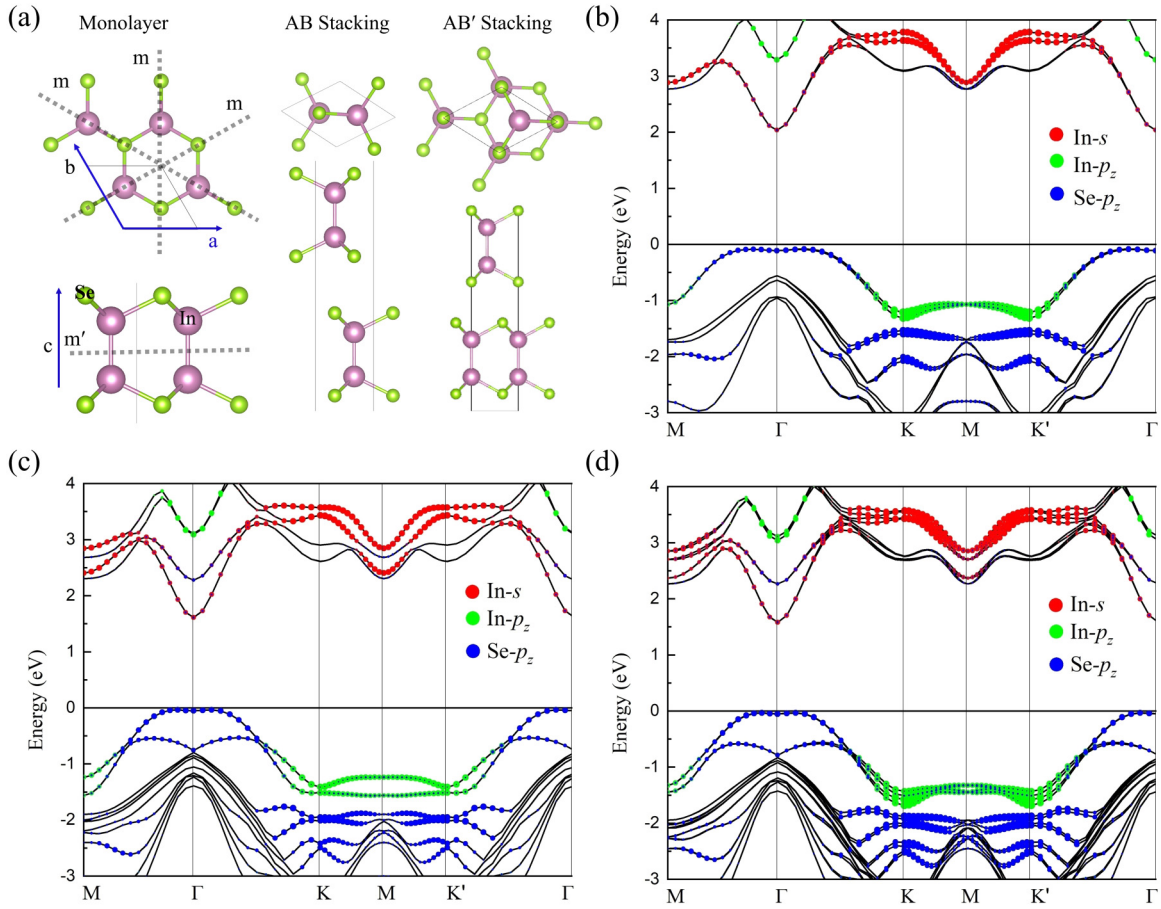

FIG. 1. Lattice and electronic structures. (a) Atomic structure with top and side view of the monolayer, *AB* and *AB*′ stackings. Projected band structure for (b) monolayer, (c) *AB* stacked bilayer, and (d) *AB*′ stacked bilayer.

strategy for spintronic and magneto-optical applications exploiting the rich physics of spin-orbit effects.

II. METHODOLOGY

We perform the density-functional theory (DFT) calculations using the projector augmented-wave method [23], including the SOC as implemented in the Vienna *Ab initio* Simulation Package (VASP) [24]. The energy cutoff of 500 eV is used for the plane-wave basis sets. The convergence criterion for energy is set to 0.001 meV. We impose a vacuum region of 15 Å in the nonperiodic direction for all calculations. All atomic positions are relaxed until the residual forces on the atoms are smaller than 0.01 eV/Å. For the accurate prediction of band gap and relativistic effect of semiconductor, the Heyd-Scuseria-Ernzerhof hybrid functional (HSE06) for exchange and correlation is used [25]. The 7 × 7 Monkhorst-Pack *k* grid is used to calculate the ground state using the HSE06 functional. Properties such as SHC require a dense *k*-point mesh to sample the BZ, which is computationally expensive. To overcome this issue, the DFT wave functions are transformed to MLWFs using the WANNIER90 package [26,27]. The spin operator expectation value matrix is estimated based on the normalized pseudo-wave function from the VASP output. The spin operator is projected on the MLWFs to calculate the spin textures and spin Hall conductivity with the converged dance *k* mesh of 200 × 200 [28,29].

III. RESULTS AND DISCUSSION

The monolayer InSe consists of two sublayers with In and Se arranged in a honeycomb lattice, as shown in Fig. 1(a). The monolayer belongs to the $P\bar{6}m2$ space group (D_{3h} point group) without inversion symmetry. This feature induces a momentum-dependent DSOC Zeeman-like field due to nonzero Berry curvature. However, the space group has 12 symmetry operations including three vertical mirror planes (m) and one horizontal mirror plane (m'). The mirror symmetries ensure the absence of electric dipole moment and RSOC interaction in the pristine monolayer. Experimentally two different phases of InSe have been reported, providing two stacking-order candidates labeled as *AB* and *AB*′ [30,31]. The *AB* stacking belongs to the $P\bar{3}m1$ space group (D_{3d} point group) with the inversion symmetry, and thus has no R/DSOC and spin splitting in its pristine form. The *AB*′ stacking is a noncentrosymmetric system of the $P3m$ space group (C_{3v} point group) with broken mirror-plane (m') symmetry, which allows the existence of both Dresselhaus and Rashba SOC components. Before going into the details of SOC interactions and SHE, we first look at the key features of electronic structures. Figures 1(b)–1(d) show the relativistic band

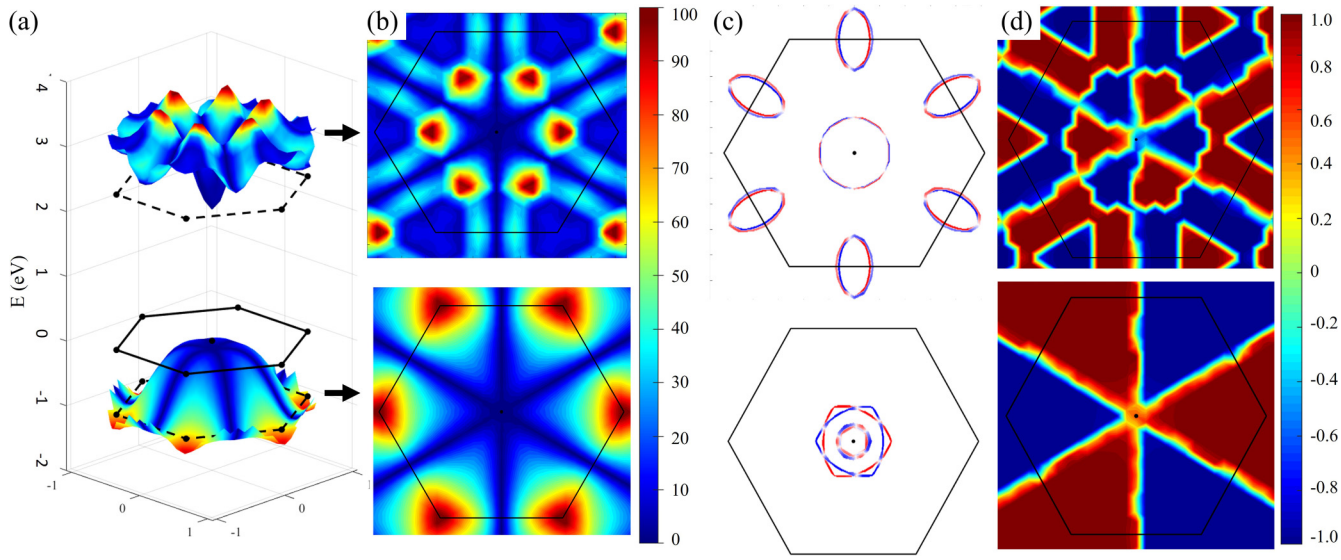

FIG. 2. DSOC interactions for the pristine monolayer InSe. (a) Three-dimensional band structure for the lowest conduction band and topmost valence band. (b) Top view of LCB (top) and TVB (bottom); color bar represents the Zeeman-like splitting in meV. (c) Fermi lines with different electron (top) and hole (bottom) doping concentrations. (d) Spin texture for LCB (top) and TVB (bottom); red and blue colors represent the positive and negative values of $\langle \pm S_z \rangle$ spin quantization, respectively.

structures of monolayer and bilayers with the orbital projections. The valence-band edge mainly originates from the In-Se p_z orbitals, and the conduction-band edge is dominated by the In(s)-Se (p_z) hybridized states. The valence-band edges have a nonparabolic Mexican-hat-like dispersion with a depression at the Γ point, and the depression is larger in the case of monolayer compared with the bilayer band structure. Overall, the band character and orbital hybridization are independent of stacking order. However, one should note that the hybridization could be modulated under the gate voltages [32,33].

The inversion asymmetry-related SOC interactions induce momentum-dependent effective magnetic field. One can explore the effects of the SOC through Zeeman-like spin splitting and momentum-dependent spin textures of electronic states [34]. Figures 2(a) and 2(b) show the 3D band structure of monolayer InSe in the full BZ, where the color map shows the SOC-induced Zeeman-like splitting in the energy scale. The largest spin splitting for the topmost valence band (TVB) (∼90 meV) is at the K (K') point, while for the lowest conduction band (LCB) the largest splitting (∼100 meV) is in the middle of the Γ-K path. The Fermi level can be tuned by charge doping to access these splittings for the transport phenomena (e.g., SHE). However, the Zeeman-like splitting around the BZ center (Γ) is minimal. Therefore, approaching the large spin splitting would require extremely high doping concentrations. The doping concentration of 10^{14} cm^{-2} for a single layer could be considered experimentally achievable. Considering the rigidity of the band dispersions under charge doping, the corresponding change in chemical potentials can be estimated through the integrated density of states. The chemical potential shift corresponding to the doping concentration of 10^{14} cm^{-2} barely achieves the spin splitting of about 11 and 23 meV for TVB and LCB, respectively. Figure 2(c) shows the Fermi lines at chemical potentials for electron and hole doping with the considered doping concentration. This shows the splitting of spin quantization $\langle \pm S_z \rangle$ at any wave vector (k) within the full BZ. The spin textures of the TVB and LCB are presented in Fig. 2(d). The wave-vector dependent spin-orbit field associated with DSOC has the form $\boldsymbol{\Omega_D} = (\boldsymbol{\nabla V} \times \boldsymbol{k})$, where $\boldsymbol{k}$ is the wave vector and $\boldsymbol{\nabla V}$ the gradient of the crystal potential. Considering that the $\boldsymbol{\nabla V}$ in InSe arises from the in-plane inversion asymmetry, and $\boldsymbol{k}$ only having in-plane components in the 2D Brillouin zone, the $\boldsymbol{\Omega_D}$ can only be an out-of-plane vector. Therefore, intrinsic DSOC creates a purely out-of-plane spin texture, and it flips with $\pi/3$ rotations due to the underlying symmetry of the atomic structure. Under the Kubo formula for linear response, the spin Hall conductivity is $\sigma_{xy}^{S_z}(\boldsymbol{k}) = \sum_n \int \frac{d^3\boldsymbol{k}}{(2\pi)^3} f_{n\boldsymbol{k}}\, \boldsymbol{\Omega}_n^z(\boldsymbol{k})$, where $\boldsymbol{\Omega}_n^z(\boldsymbol{k}) = \sum_{m\neq n} \frac{2Im\ \langle\psi_{n\boldsymbol{k}}|j_x|\psi_{m\boldsymbol{k}}\rangle\langle\psi_{m\boldsymbol{k}}|v_y|\psi_{n\boldsymbol{k}}\rangle}{(E_m - E_n)^2}$, $f_{n\boldsymbol{k}}$ is the Fermi-Dirac distribution function, $\psi_{\boldsymbol{k}}$ are Bloch states, E represents the eigenvalues, v_x and j_x are the velocity and spin-current operators, respectively. In a two-dimensional material, only the in-plane spin Hall conductivity with out-of-plane magnetization (S_z) will be considered [28]. Therefore, the DSOC induced out-of-plane persistent spin textures are considered ideal for SHE application [35,36].

In the presence of SOC, the spin current (j_x) at any wave vector is dependent on the spin angular moment (S) as well as the orbital angular moment (L). Therefore, the nature of SOC plays a crucial role in determining the momentum-dependent spin polarization. It is hard to manipulate DSOC externally as it is a purely intrinsic phenomenon that depends on crystal asymmetry. In contrast, RSOC could be easily introduced and manipulated through gate voltages. The gate voltage breaks m' mirror symmetry by charge redistribution and electric dipole moment. The electric field-induced charge redistribution at 1.0 eV/Å is shown in Fig. 3(a). Figure 3(b) shows the band dispersions along the M-Γ-K path at different gate voltages. The Zeeman-like spin splitting around Γ increases with the applied gate voltage. Furthermore, the spin degeneracy breaks up even along the M-Γ path due to the RSOC. This can be

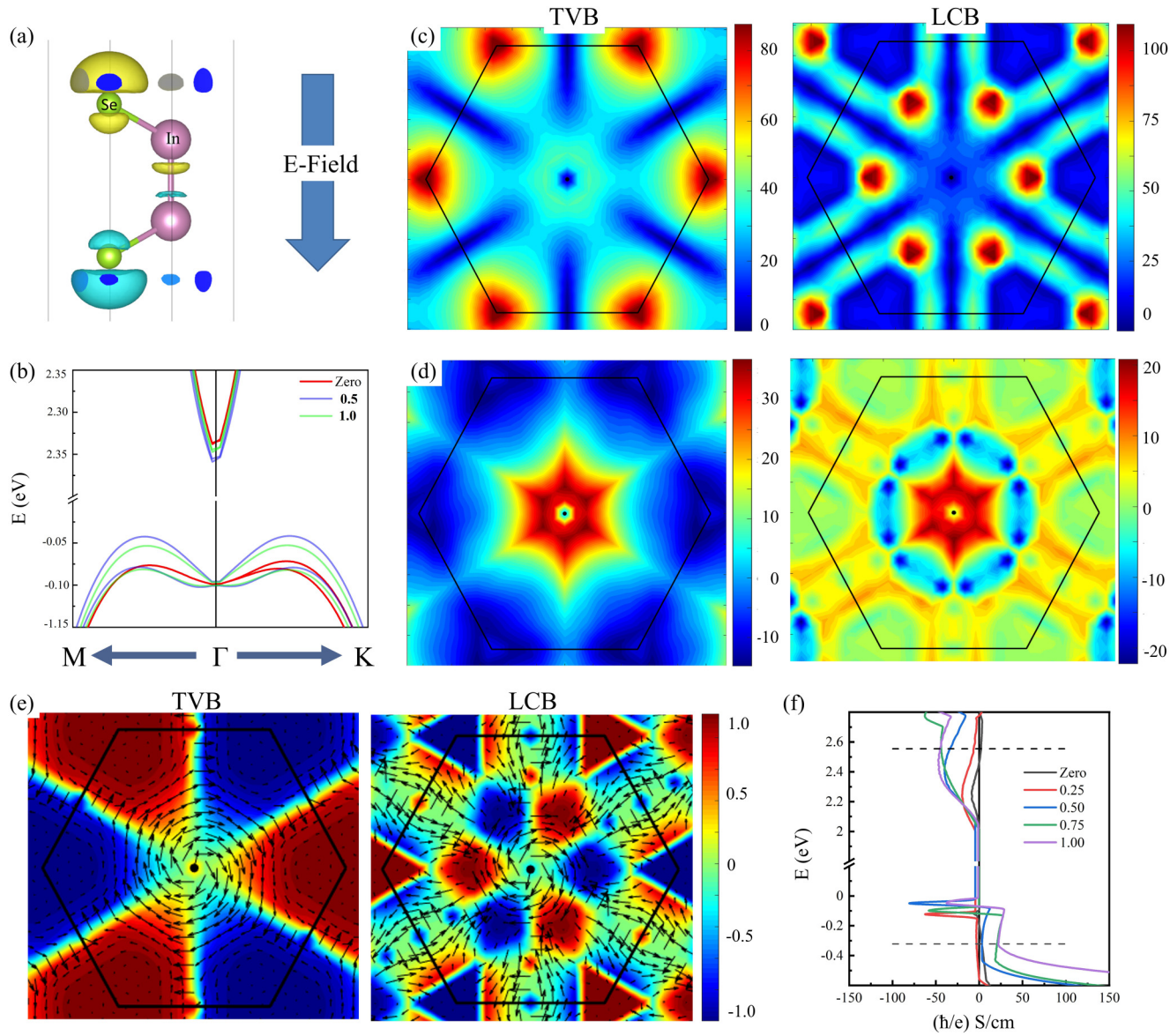

FIG. 3. Interplay between DSOC and the electric field-induced RSOC in monolayer InSe. (a) Charge redistribution under the gate voltage of 1.0 eV/Å, where yellow and cyan color represent charge accumulation and reduction. (b) Band dispersion around Γ along M-Γ-K path with different gate voltages in units of eV/Å. (c) Total Zeeman-like splitting in the full BZ for TVB (left) and LCB (right) at an electric field of 1.0 eV/Å. (d) Zeeman-like splitting of TVB (left) and LCB (right) induced only by RSOC at the electric field of 1.0 eV/Å. (e) Spin textures for TVB (left) and LCB (right) at the electric field of 1.0 eV/ Å, where the spin at each k point is normalized. Color bar represents the out-of-plane component of spin quantization, while the arrows indicate the in-plane spin component. (f) SHC with change in chemical potential at different gate voltages. Dashed line representing the carrier concentration of 10^{14} cm^{-2}.

further clarified in the contour plot of the Zeeman-like splitting for TVB and LCB at a gate voltage of 1.0 eV/A, as shown in Fig. 3(c). It can be seen that a significant spin splitting of ∼40 meV around Γ occurs in an isotropic manner. The total spin splitting is the sum of the contributions induced by DSOC and RSOC. Therefore, the net effect of RSOC can simply be deduced by subtracting the Zeeman splitting at zero field from that at finite gate voltages. The calculated RSOC-induced Zeeman-like splitting at the electric field of 1.0 eV/Å is shown in Fig 3(d). In the case of TVB, the RSOC Zeeman-like splitting is positive (∼30 meV) around the BZ center (Γ), while it is negative at the corners (K/K'). Similarly, one can see an increase of ∼20 meV for LCB around Γ with the reduction in other parts of the BZ. This presents an interesting picture of the interplay between the two types of SOC interactions. In the presence of DSOC, RSOC does not simply add up in the Zeeman-like splitting. Instead, the introduction of RSOC just shifts the splitting at the center of the BZ. This makes access to this Zeeman-like splitting more achievable through electron/hole doping and optical excitations. The spin textures for LCB and TVB under the electric field of 1.0 eV/Å are shown in Fig. 3(e). The purely out-of-plane persistent spin texture is transformed into the canted spin texture. We have calculated the percentage of in-plane spin component as $S_P = \frac{\sum_{k=1}^{N} S_k}{N} \times 100\%$, where S_k is in-plane spin component at each k point, and N is the total number of k points. The

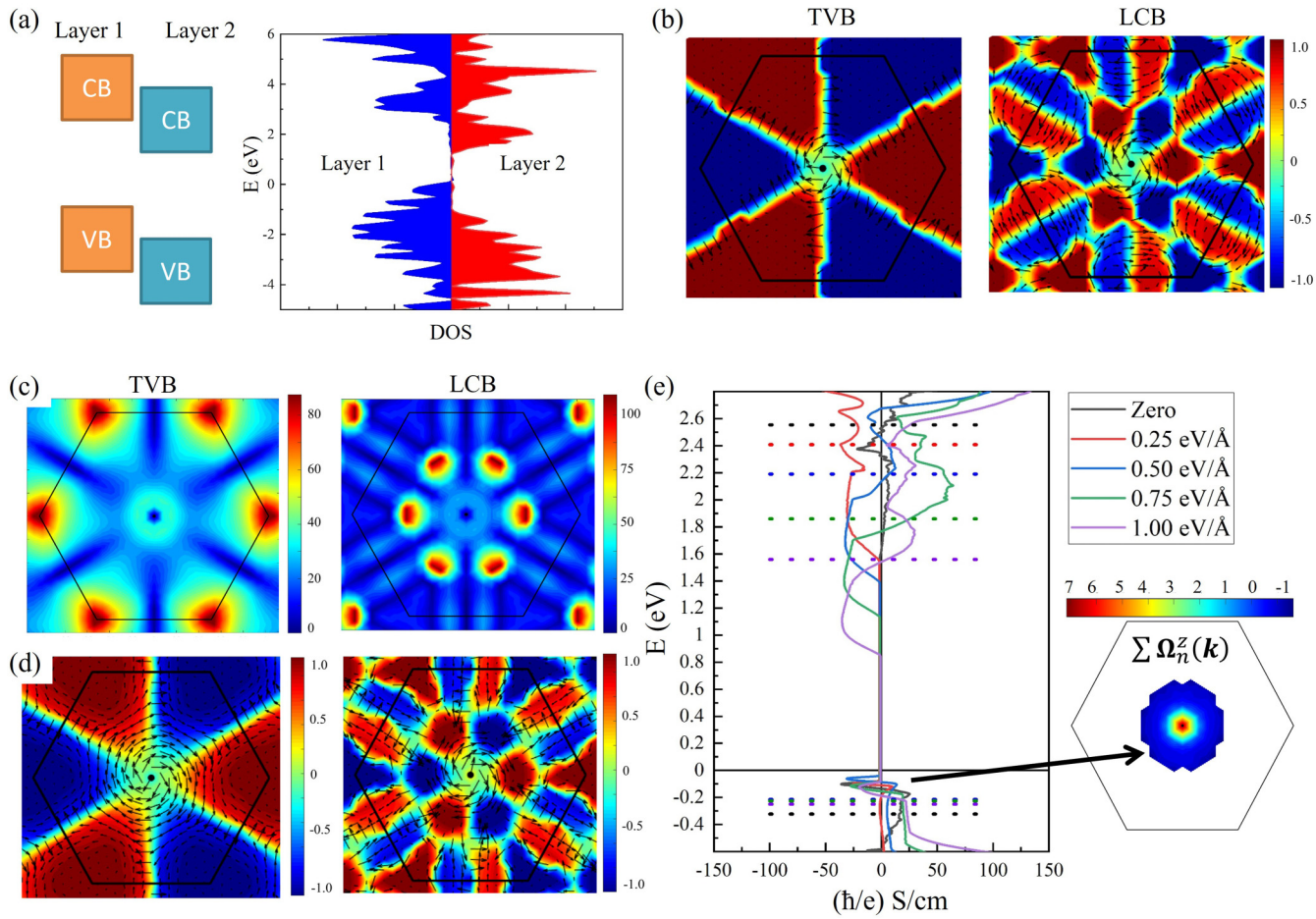

FIG. 4. Electric field-induced RSOC in *AB* stacked bilayer. (a) Schematics for the decoupling of states under the gate voltages (right) and the decomposed density of state for layer 1 and layer 2 (left). (b) The spin textures for TVB (left) and LCB (right) in the whole BZ of *AB* stacked bilayer at the electric field of 0.25 eV/Å. (c) Spin splitting at the electric field of 1.0 eV/Å in units of meV. (d) Spin textures at the electric field of 1.0 eV/Å. Colors and relative ratios of vector length are same as shown in Fig. 3. (e) SHC as a function of the chemical potential at different gate voltages. The dashed lines represent the doping concentration of 10^{14} cm^{-2}. Plot on the right represents $\sum \boldsymbol{\Omega}_n^z(\boldsymbol{k})$ around the Γ point at zero field, where n includes the two highest valence bands.

calculated values at electric field of 1.0 eV/ Å are 34 and 53% for TVB and LCB, respectively. Since the electron moving through a dipole field feels a RSOC magnetic field of the form $\boldsymbol{\Omega_R} = (\boldsymbol{E} \times \boldsymbol{k})$, where $\boldsymbol{E}$ is the electric dipole field and $\boldsymbol{k}$ is the wave vector. Given that the electric dipole field is out-of-plane, the in-plane momentum-dependent RSOC field is formed, which gives rise to an in-plane spin component. The stronger the RSOC-induced Zeeman splitting [Fig. 3(b)], the stronger the in-plane spin component. It is interesting to check the effect of gate voltage on the SHC. The SHC can be calculated by using the Kubo formula as discussed above. Figure 3(f) shows the spin Hall effect of $\langle \pm S_z \rangle$ magnetic quantization with the change in the chemical potentials mimicking the charge (electron/hole) doping. The effective chemical potentials for the considered charge-doping concentrations are indicated with dashed lines. Without the gate voltage, the SHC value is small with a high peak present near the valence-band edge, which is attributed to the Mexican-hat feature of TVB. The SHC increases significantly with the application of gate voltage up to 0.5 eV/Å. However, with the further increase in the gate voltage, the value of SHC is stalled. This is surprising considering the fact that the Zeeman-like splitting within the energy range increases consistently with the increasing gate voltage up to 1.0 eV/Å. Note that the RSOC introduces two competing factors: one is the increase in the Zeeman-like splitting around Γ, which contributes to increasing the SHC, and the other is the transformation of the spin texture from out-of-plane to in-plane spin quantization, which counteract by reducing the $\langle \pm S_z \rangle$ spin component. At the gate voltage of 0.5 eV/Å, these two factors balance each other, leading to a stall in the enhancement of the intrinsic SHC.

Now we discuss the centrosymmetric bilayer with the *AB* stacking [Fig. 1(a)]. While the stacking order breaks the m' mirror symmetry, the inversion symmetry ensures the absence of both DSOC and RSOC interactions. Under gate voltages, the system transforms into an inversion asymmetric C_{3v} point group with the three mirror symmetries (m). The applied gate voltage creates a potential gradient across layers and causes decoupling of the states belonging to different layers. For instance, if the electric field is applied in the direction from layer 1 to 2, the states from layer 1 gain energy, while the states of layer 2 lower the energy, and thus the band gap gradually decreases with increasing gate voltage. Figure 4(a)

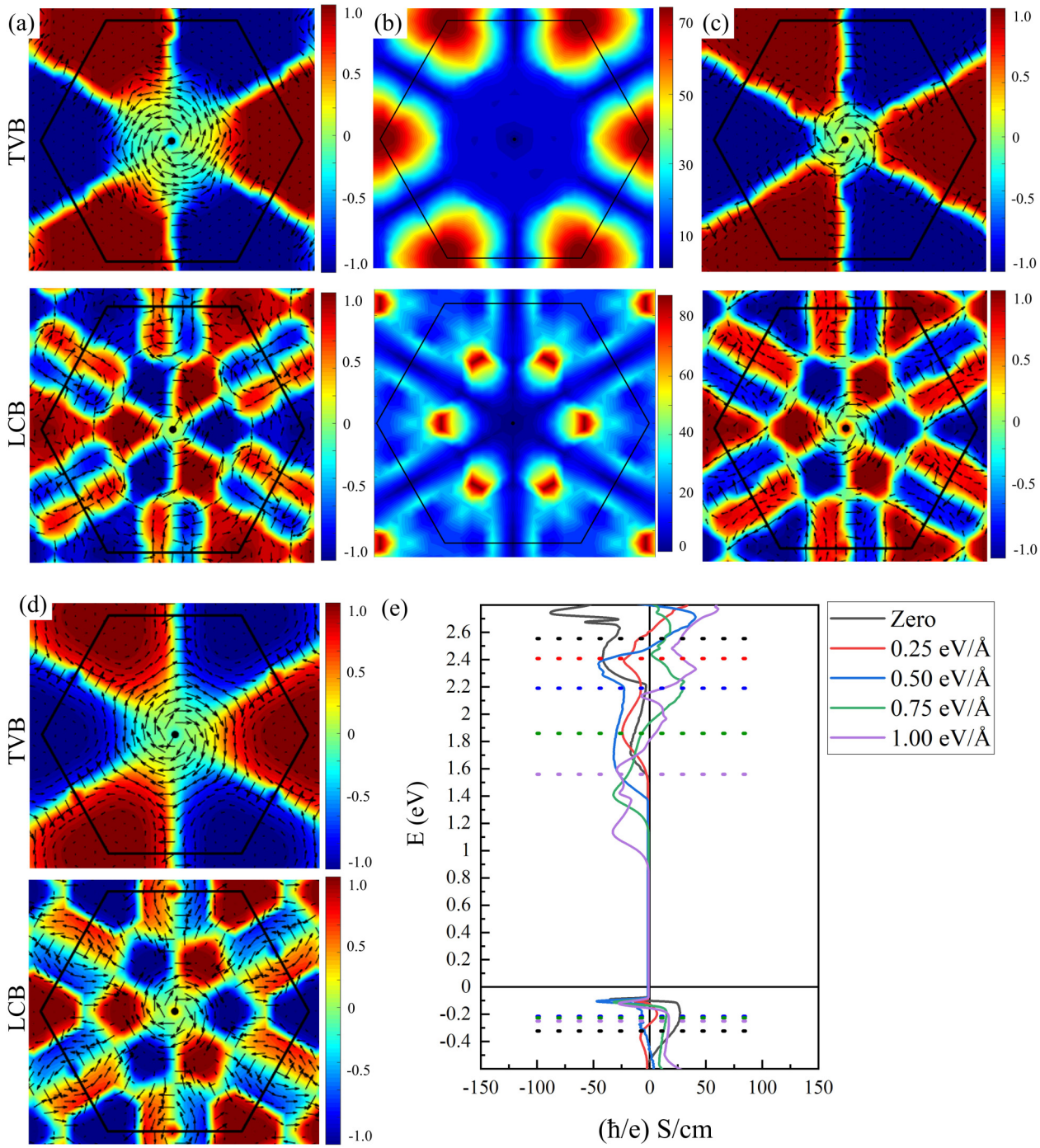

FIG. 5. RSOC in AB' stacked bilayer. (a) Spin textures for TVB (top) and LCB (bottom) in the whole Brillouin zone of AB' stacked bilayer InSe with no external electric field. (b) Spin splitting in unit of meV. (c), (d) Spin textures at the electric field of 0.5 and 1.0 eV/Å for the TVB (top) and LCB (bottom), respectively. Colors and relative ratios of vector length are same as shown in Fig. 3. (e) SHC as a function of the chemical potential at different gate voltages. Dashed lines denote the Fermi level with a doping concentration of 10^{14} cm^{-2}.

shows the partial density of states for the two layers at a gate voltage of 1.0 eV/Å. Here, the states for TVB belong to layer 1, while LCB has the states from layer 2. Therefore, the in-plane crystal inversion asymmetry of the individual layer comes into play. Figure 4(b) shows the spin textures for TVB and LCB under a small electric field of 0.25 eV/Å, and the average in-plane spin component is only about 15% for TVB and 28% for LCB. The stronger out-of-plane spin character suggests that the DSOC is a dominant factor at small gate voltage. Figures 4(c) and 4(d) show the Zeeman-type splitting and spin textures under an electric field of 1.0 eV/Å; the average in-plane spin component increases to 50 and 41%, for TVB and LCB, respectively. The spin textures and Zeeman splitting around Γ are almost identical to the monolayer counterpart under gate voltages of 1.0 eV/Å [see Figs. 3(c) and 3(e)]. Figure 4(e) shows the SHC with respect to the

chemical potential at different gate voltages. As mentioned earlier, the potential gradient across the layers has reduced the effective band gap. In general, the SHC values without gate voltages are small within the considered energy range. It is important to note that a high peak of the SHC around the valence-band edge presents even without gate voltages for the centrosymmetric system. This is essentially due to the SHE contributed by the orbital angular momentum [37]. The spin Berry curvature $[\sum_{n=1,2} \mathbf{\Omega}_n^z(\boldsymbol{k})]$ for the two highest nondegenerated valence bands around the Γ point at zero field is also shown in Fig. 4(e). The positive contribution to the SHC coincides with the van Hove singularity of the Mexican-hat feature of the TVB. Although the peak related to the Mexican hat stays approximately the same, the SHC in general significantly increases with the gate voltage up to 0.5 eV/Å. As of the monolayer case, the absolute peak values of SHC are almost unchanged with the further increase of the gate voltages.

Unlike the *AB* stacking, the *AB*′ stacking has inversion asymmetry, and the m' mirror symmetry is broken. This implies that *AB*′ stacking harbors both DSOC and RSOC even without an external perturbation such as external electric fields. Figures 5(a) and 5(b) show the spin textures and Zeeman splitting without gate voltage. The TVB and LCB have an average in-plane spin component of about 29 and 42%, respectively. The intrinsic RSOC drives a spin spiral character around the Γ point and an out-of-plane spin texture at the edges of the BZ occurs due to DSOC. In this case, the intrinsic RSOC and related spin texture are attributed to strong interlayer couplings and the lack of mirror symmetry (m') [20]. Figure 5(c) shows the spin textures for the TVB and LCB at the electric field of 0.5 eV/Å. The in-plane spin component reduces to 12% for TVB and 20% for LCB, respectively. With the application of a small gate voltage, the in-plane spin texture of TVB squeezes around the Γ point, while the out-of-plane spin component expands in the BZ and the spin spiral direction switches from anticlockwise to clockwise for both TVB and LCB. The states belonging to different layers are decoupled under the gate voltages, and the spin spiral direction is dominated by the electric field-induced RSOC, rather than the intrinsic effect. This shows that the RSOC and spin spiral direction can be tuned by the electric field-induced decoupling of the states belonging to different layers. At the electric field of 1.0 eV/Å, the in-plane spin components for TVB and LCB are again spread to 35 and 40%, respectively [Fig. 5(d)]. Figure 5(e) shows the SHC in the *AB*' stacked bilayer InSe. It can be seen that the value of SHC in the *AB*' stacking at zero electric field is comparable to that in monolayer and *AB* stacking case under the electric field of 0.5 eV/Å. These findings demonstrate a great prospect for the development of electric-controllable chirality-based spintronic devices.

IV. SUMMARY

In summary, we have presented the study of the modulation of SOC interactions through stacking order and gate voltage in mono- and bilayer InSe. The character of the interplay between Dresselhaus and Rashba SOC interactions and their impacts on SHE have been investigated. The monolayer InSe exhibits a persistent out-of-plane spin texture due to the DSOC associated with the inversion asymmetry of the atomic structure. The band dispersions with opposite spin states at the BZ center are nearly degenerated, while a larger Zeeman-like splitting occurs at the BZ corners. In the presence of DSOC, the introduction of RSOC does not directly enhance the Zeeman-like spin splitting. However, it shifts the splitting from the corners to the center of the BZ, which contributes to the enhancement of SHC. On the other hand, the RSOC can induce a momentum-dependent in-plane tilting of spin quantization. Due to the two competing factors, the enhancement of SHC ($\sigma_{xy}^{s_z}$) gets saturated when the applied electric field is larger than 0.5 eV/Å. The centrosymmetric *AB* stacked bilayer without gate voltages shows a SHC peak associated with the Mexican-hat-like valence-band edge. We also investigate the coexistence of RSOC and DSOC interactions in the *AB*′ stacking. The strong interlayer interactions create a spin spiral map comparable to the field-induced spin spiral textures of a monolayer and *AB* bilayer. Quantitatively, the stacking order-induced RSOC produces the same effects for SHC as of the electric field-induced RSOC. Moreover, at small gate voltages, the decoupling of the states belonging to different layers enables the switching of spin momentum locking, where spin spiral direction changes from anticlockwise with no field to clockwise under gate voltages. Our study suggests that RSOC induced by an electric field or stacking order contributes to the enhancement of SHE by enhancing the Zeeman-like splitting around Γ. This manipulation of the spin texture in 2D materials provides a promising route for spintronic and magneto-optical applications exploiting the rich physics of spin-orbit effects.

ACKNOWLEDGMENTS

Work at SUSTech was supported by the National Natural Science Foundation of China under Grant No. 11774142, and the Shenzhen Basic Research Fund under Grant. No. JCYJ20180504165817769. The computer time was supported by the Center for Computational Science and Engineering of Southern University of Science and Technology.

[1] H. Sawahata, N. Yamaguchi, H. Kotaka, and F. Ishii, Jpn. J. Appl. Phys. **57**, 030309 (2018).
[2] M. U. Farooq, A. Hashmi, T. Ono, and L. Huang, npj Comput Mater **6**, 1 (2020).
[3] N. P. Armitage, E. J. Mele, and A. Vishwanath, Rev. Mod. Phys. **90**, 015001 (2018).
[4] Y.-M. Xie, B. T. Zhou, and K. T. Law, Phys. Rev. Lett. **125**, 107001 (2020).
[5] N. Nagaosa, J. Sinova, S. Onoda, A. H. MacDonald, and N. P. Ong, Rev. Mod. Phys. **82**, 1539 (2010).
[6] J. Sinova, S. O. Valenzuela, J. Wunderlich, C. H. Back, and T. Jungwirth, Rev. Mod. Phys. **87**, 1213 (2015).

[7] T. Kampfrath, M. Battiato, P. Maldonado, G. Eilers, J. Nötzold, S. Mährlein, V. Zbarsky, F. Freimuth, Y. Mokrousov, S. Blügel, M. Wolf, I. Radu, P. M. Oppeneer, and M. Münzenberg, Nat. Nanotechnol. **8**, 256 (2013).

[8] S.-Q. Shen, Y.-J. Bao, M. Ma, X. C. Xie, and F. C. Zhang, Phys. Rev. B **71**, 155316 (2005).

[9] C. Sun, H. Yang, and M. B. A. Jalil, Phys. Rev. B **102**, 134420 (2020).

[10] Y. Du, H. Gamou, S. Takahashi, S. Karube, M. Kohda, and J. Nitta, Phys. Rev. Applied **13**, 054014 (2020).

[11] C. K. Safeer, J. Ingla-Aynés, N. Ontoso, F. Herling, W. Yan, L. E. Hueso, and F. Casanova, Nano Lett. **20**, 4573 (2020).

[12] M. Zhou, S. Yu, W. Yang, W. K. Lou, F. Cheng, D. Zhang, and K. Chang, Phys. Rev. B **100**, 245409 (2019).

[13] J. Zhou, J. Qiao, A. Bournel, and W. Zhao, Phys. Rev. B **99**, 060408(R) (2019).

[14] K. Taguchi, D. Oshima, Y. Yamaguchi, T. Hashimoto, Y. Tanaka, and M. Sato, Phys. Rev. B **101**, 235201 (2020).

[15] A. Ceferino, S. J. Magorrian, V. Zólyomi, D. A. Bandurin, A. K. Geim, A. Patanè, Z. D. Kovalyuk, Z. R. Kudrynskyi, I. V. Grigorieva, and V. I. Fal'ko, Phys. Rev. B **104**, 125432 (2021).

[16] M. Zhou, D. Zhang, S. Yu, Z. Huang, Y. Chen, W. Yang, and K. Chang, Phys. Rev. B **99**, 155402 (2019).

[17] L. Du, T. Hasan, A. Castellanos-Gomez, G.-B. Liu, Y. Yao, C. N. Lau, and Z. Sun, Nat. Rev. Phys. **3**, 193 (2021).

[18] J. Yan, J. Xia, X. Wang, L. Liu, J.-L. Kuo, B. K. Tay, S. Chen, W. Zhou, Z. Liu, and Z. X. Shen, Nano Lett. **15**, 8155 (2015).

[19] K. Iordanidou, M. Houssa, J. Kioseoglou, V. V. Afanas'ev, A. Stesmans, and C. Persson, ACS Appl. Nano Mater. **1**, 6656 (2018).

[20] Y. Sun, S. Luo, X.-G. Zhao, K. Biswas, S.-L. Li, and L. Zhang, Nanoscale **10**, 7991 (2018).

[21] H. Cai, Y. Gu, Y.-C. Lin, Y. Yu, D. B. Geohegan, and K. Xiao, Appl. Phys. Rev. **6**, 041312 (2019).

[22] K. Yasuda, X. Wang, K. Watanabe, T. Taniguchi, and P. Jarillo-Herrero, Science **372**, 1458 (2021).

[23] P. E. Blöchl, Phys. Rev. B **50**, 17953 (1994).

[24] G. Kresse and J. Furthmüller, Comput. Mater. Sci. **6**, 15 (1996).

[25] A. V. Krukau, O. A. Vydrov, A. F. Izmaylov, and G. E. Scuseria, J. Chem. Phys. **125**, 224106 (2006).

[26] A. A. Mostofi, J. R. Yates, G. Pizzi, Y.-S. Lee, I. Souza, D. Vanderbilt, and N. Marzari, Comput. Phys. Commun. **185**, 2309 (2014).

[27] G. Pizzi, V. Vitale, R. Arita, S. Blügel, F. Freimuth, G. Géranton, M. Gibertini, D. Gresch, C. Johnson, T. Koretsune, J. Ibañez-Azpiroz, H. Lee, J.-M. Lihm, D. Marchand, A. Marrazzo, Y. Mokrousov, J. I. Mustafa, Y. Nohara, Y. Nomura, L. Paulatto, S. Poncé, T. Ponweiser, J. Qiao, F. Thöle, S. S. Tsirkin, M. Wierzbowska, N. Marzari, D. Vanderbilt, I. Souza, A. A. Mostofi, and J. R. Yates, J. Phys.: Condens. Matter **32**, 165902 (2020).

[28] J. Qiao, J. Zhou, Z. Yuan, and W. Zhao, Phys. Rev. B **98**, 214402 (2018).

[29] J. H. Ryoo, C.-H. Park, and I. Souza, Phys. Rev. B **99**, 235113 (2019).

[30] J. Rigoult, A. Rimsky, and A. Kuhn, Acta Crystallogr., Sect. B **36**, 916 (1980).

[31] G. V. Lashkarev, V. V. Slynko, Z. D. Kovalyuk, V. I. Sichkovskyi, M. V. Radchenko, P. Aleshkevych, R. Szymczak, W. Dobrowolski, R. Minikaev, and A. V. Zaslonkin, Mater. Sci. Eng. C **27**, 1052 (2007).

[32] Y. Y. Liang, H. Chen, H. Mizuseki, and Y. Kawazoe, J. Chem. Phys. **134**, 144113 (2011).

[33] J. Kammhuber, M. C. Cassidy, H. Zhang, Ö. Gül, F. Pei, M. W. A. de Moor, B. Nijholt, K. Watanabe, T. Taniguchi, D. Car, S. R. Plissard, E. P. A. M. Bakkers, and L. P. Kouwenhoven, Nano Lett. **16**, 3482 (2016).

[34] C. Mera Acosta, A. Fazzio, and G. M. Dalpian, npj Quantum Mater. **4**, 1 (2019).

[35] L. L. Tao and E. Y. Tsymbal, Nat. Commun. **9**, 2763 (2018).

[36] H. Ai, X. Ma, X. Shao, W. Li, and M. Zhao, Phys. Rev. Mater. **3**, 054407 (2019).

[37] D. Go, D. Jo, C. Kim, and H.-W. Lee, Phys. Rev. Lett. **121**, 086602 (2018).